Electronic Supplementary Information (ESI)

Size-modulation of functionalized Fe_3O_4: Nanoscopic customization to devise resolute piezoelectric nanocomposites

Souvik Bhattacharjee,[a] Nilesh Mazumder,[a,‡] Suvankar Mondal,[a] Karamjyoti Panigrahi,[b] Anibrata Banerjee,[b] Dimitra Das,[b] Saikat Sarkar,[a] Dipayan Roy,[b] and Kalyan Kumar Chattopadhyay[a,b,*]

[a]Department of Physics, Jadavpur University, Kolkata – 700 032, India

[b]School of Materials Science and Nanotechnology, Jadavpur University, Kolkata – 700 032, India

[‡]Present Affiliation: Govt. College of Engineering & Ceramic Technology, Kolkata – 700 010, India

*E-mail: kalyan_chattopadhyay@yahoo.com; Fax: +91 33 2114 6584; Phone: +91 33 2413 8917.

ORCID:

Souvik Bhattacharjee: https://orcid.org/0000-0003-0329-3171

Karamjyoti Panigrahi: https://orcid.org/0000-0002-1568-7234

Kalyan Kumar Chattopadhyay: https://orcid.org/0000-0002-4576-2434

Table of Contents

1. Synthesis

1.1. Approach

Extensive literature survey reveals a wide variety of bottom-up magnetite synthesis methods including co-precipitation,[1,2] sol–gel technique,[3] one-pot synthesis with reflux or hot-injection method in inert condition,[4-6] electrochemical,[7] solvothermal or hydrothermal,[8-10] reduction followed by microwave irradiation,[11,12] thermal decomposition of iron (III) acetylacetonate[13] etc. Use of different bases, reducing and capping agents such as NaOH, KOH, $NaBH_4$, $N(CH_3)_4OH$, sodium oleate and polymers (PEG, PVA, PVP, PAA etc) for ligand exchange or post-synthetic functionalization over the existing ligand coating have been reported previously.[14,15] Jun *et al.* developed biocompatible Fe_3O_4 nanocrystalline samples by using 2,3-dimercaptosuccinic acid (DMSA) as a capping ligand to study size-dependent magnetic properties for MFH & MRI-based applications.[16] The effect of size, shape, morphology and surface functionalization in different physio-chemical properties have been thoroughly scrutinized by many researchers. Actually, any air exposure to magnetite's nanoscopic surface having high chemical reactivity promotes partial oxidation to maghemite.[17] As described by da Costa *et al*., once oxidation begins at the surface, it eventually extends to the entire particle volume. In distinct works, polyol-mediated synthesis is considered one of the most promising and multipurpose method to obtain high-quality crystalline nanoparticles and adapted in this work. It is a versatile chemical approach to prepare water-stable MNPs, where an even mixture of ethylene glycol (EG), diethylene glycol (DEG), triethylene glycol (TREG), tetraethylene glycol (TEG) and poly(ethylene glycol) (PEG) of different molecular weights are used as a high boiling-point solvent, reductant, and stabilizer to control morphology, particle growth and interparticle aggregation.[18]

1.2. Microwave synthesis reactor and its implication

Fe_3O_4 nanoparticles are synthesized in the single-mode Anton-Paar microwave reactor-Monowave 200. The system operates at a frequency of 2.45 GHz with a maximum power of 850 W. Pressure and temperature can be simultaneously monitored by an external infrared (IR) sensor and an internal fibre-optic (FO) probe. With this system, glass-vials of 2 different size (G10 & G30; the number represents the maximum capacity of the vial in mL) and one Silicon Carbide

(SiC) vial (C10) are supplied. Only SiC vials are suitable for this synthesis protocol in order to prevent accidents during reactions at the maximum values of temperature (T_{max} = 260°C) and pressure (P_{max} = 30 bar).

In traditional solvothermal routes, the precursor-solution is directly transferred to a teflon-lined stainless still jacket and placed to be heated in a hot-air oven for hours or even days. However homogeneous and well-dispersed the precursors are, eventually undergoes some density distribution inside; besides due to finite thermal conductivity of the container as well as the precursor-medium, the part of the solution in direct touch with the teflon-wall attains the required temperature first and then it slowly gets conducted to the interior region. Naturally, seed-crystals get created first at the exterior region, and by the time the interior-part reaches the set-temperature, the outer seeds already grow to a certain extent. Moreover, the growth-dynamics hugely depend on the local density of the precursors. Hence, particles of a broad size-distribution are formed, which is hardly suitable for size-dependent studies like this work. The best way to acquire uniform nucleation & growth is continuous stirring to cease any density or temperature-gradient; which is followed in one-pot, hot injection or reflux methods. In microwave synthesis reactor the magnetic beed can be rotated upto 1200 rpm, higher than that of the traditional one-pot set-ups; generating an extremely narrow size-distribution of the nanoparticles in a very short span of time.

1.3.Chemical reactions

The polyol solvent supplies adequate amount of OH^- ions in the solution in presence of CH_3COONa. This makes up the required reducing environment for the nucleation of Fe_3O_4 nanocrystallites. In the first step iron hydroxides and goethite (α-FeOOH) form. Then Fe_3O_4 is generated by a solid-state reaction between them in definite temperature, pressure, reaction/crystal-growth time *etc*. The reactions follow:

$$FeCl_3 \rightarrow Fe^{3+} + 3Cl^-$$

$$Fe^{3+} + 3OH^- \rightarrow Fe(OH)_3$$

$$Fe^{3+} + e^- \rightarrow Fe^{2+}$$

$$Fe^{2+} + 2OH^- \rightarrow Fe(OH)_2$$

$$Fe(OH)_3 \rightarrow \alpha - FeOOH + H_2O$$

$$Fe(OH)_2 + 2\alpha - FeOOH \rightarrow Fe_3O_4(\downarrow) + 2H_2O$$

1.4.Synthesis details: precautions and parameters

- It is essential to centrifuge and wash the samples in a balanced mixture of deionized water and absolute ethanol; having solubility enough to keep sodium tartrate in dissolved state and allow the as-synthesized water-dispersible MNPs to precipitate out during centrifugation. Otherwise in pure aqueous solution, MNPs remain dispersed even against 15000 rpm – 1°C for at least half an hour. This represents the high dispersibility of the functionalized MNPs in water.
- Drying in open air might compromise the sample-quality due to partial oxidation to specific phases of Fe_2O_3.
- It is cautionary that, the heating profile with the maximum power of 850 W is prohibited for SiC vials having a thermal conductivity large enough to exceed the maximum temperature limit inside the microwave reactor.

Different synthesis-parameters, concentration of precursor & surfactants and related details are listed in Table S1 for persistent reproduction of samples.

Table S1. Synthesis-parameters, particle dimensions, ZP-vales and optical band-gap for all samples

Reaction-temperature (°C)	Synthesis technique	Sample Code	Amount of reagents					Growth-time	Crystallite-size (d_{WH}) in nm from W-H plot	Hydrodynamic size (d_H) in nm from DLS	Average particle-diameter (d_{EM}) in nm from SEM/TEM	(-) Zeta Potential in mV	Optical Band-gap (E_g) in eV
			EG + DEG (ml)	$FeCl_3.6H_2O$ (gm)	Sodium tartrate (gm)	Sodium acetate (gm)	PEG - 6000 (gm)						
220 (Series – A)	Microwave assisted solvothermal	A1	25+0	0.50	0.02	1.75	1.00	2 h	50.3 ± 2.1	X	53.2 ± 1.1	10.7	2.61
		A2	20+5	0.40	0.03	1.60	1.20	1 h	38.9 ± 5.1	47.1 ± 1.4	39.8 ± 0.9	20.1	2.99
		A3			0.04	1.50	1.30	50 min	29.4 ± 2.6	X	33.0 ± 1.8	23.9	3.60
		A4	15+10		0.06	1.40	1.40	40 min	10.7 ± 3.0		11.9 ± 0.6	28.7	4.00
		A5	10+15		0.10	1.30	1.50	30 min	7.6 ± 3.2		7.9 ± 0.8	35.3	4.24
		A6	5+20	0.35	0.15	1.20	1.60	22 min	4.3 ± 3.0	9.2 ± 0.5	5.5 ± 1.0	38.3	4.78
200 (Series – B)		B1	25+0	0.50	0.02	1.75	1.00	2 h	45.0 ± 1.0	X	48.9 ± 0.7	X	2.72
		B2	20+5	0.40	0.03	1.60	1.20	1 h	32.2 ± 1.9		30.2 ± 1.2		3.67
		B3			0.04	1.50	1.30	50 min	15.1 ± 3.0	21.2 ± 0.9	16.0 ± 1.4		3.80
		B4	15+10		0.06	1.40	1.40	40 min	8.9 ± 2.9	X	9.1 ± 0.4		4.08
		B5	10+15		0.10	1.30	1.50	30 min	6.0 ± 3.4		7.0 ± 0.8		4.34
		B6	5+20	0.35	0.15	1.20	1.60	22 min	2.9 ± 2.2		3.7 ± 0.4		4.92
185 (Series – C)	Ordinary solvothermal	C1	30+10	1.00	0.05	4.00	1.00	32 h	202.0 ± 0.4	223.7 ± 6.9	242.8 ± 2.4		1.59
		C2	20+20	0.90	0.10	3.00	2.00	16 h	119.8 ± 0.4	X	127.1 ± 0.5		1.88
		C3	10+30	0.80	0.15	2.00	3.00	8 h	86.0 ± 1.9	88.8 ± 5.2	84.5 ± 1.2		2.26
S		Commercial powder purchased from SIGMA-ALDRICH							40.5 ± 0.3	X	43.9 ± 0.2		2.30

"X" means, experiment has not been conducted.

2. Characterization techniques and specifications

The crystallographic phase composition of the as-synthesized samples is determined from X-ray diffraction using Rigaku Miniflex powder X-ray diffractometer; operated at 40kV−15mA. Data is acquired in steps of 0.02° at a rate 1°/min. Surface morphology and size-distribution of MNPs are analysed using a field emission scanning electron microscope (FESEM, JEOL 6340F FEG-SEM), whereas a high-resolution transmission electron microscope (HRTEM, JEOL-JEM 2100) operated at 200 kV; is employed to observe the ultra-small nanoparticles, analyse crystalline nature and unidirectional growth. Samples for FESEM and HRTEM are prepared by casting a drop of dilute dispersion in ethanol on Si wafer and Ted Pella carbon type-B support films (200 mesh grids) respectively, followed by fast evaporation.

The hydrodynamic particle-size (d_H) is determined from DLS-nano ZS90 (Zetasizer Nanoseries, Malvern Instruments) using a dilute solution (~0.1 g L^{-1}), prepared by ultrasonicating the powder-sample in distilled water. The incident laser is projected at an angle 173° for detecting backscattered photons and the average size is estimated from the autocorrelation function of the time-dependent fluctuation in scattered intensity. Particles in a colloidal dispersion scatter the incident laser, so the scattered intensity continuously fluctuates over time due to Brownian motion of the mobile particles and get detected in DLS instrument. Generally, particles having dimensions $\leq \lambda/_{10}$, λ being the wavelength of the incident light, scatter light elastically and isotropically (Rayleigh scattering).[19] However, when the size exceeds this threshold of $\lambda/_{10}$, Rayleigh scattering is dominated by anisotropic (preferably in forward and backward direction) Mie scattering. As particle-size further increases, Mie scattering predominantly takes place in the forward direction. Hence, by generating an autocorrelation function (ACF) based on time-variation of intensity and degree of anisotropy of the scattered light, number-distribution of particle-size is estimated in DLS. Both d_H and ζ-potential are evaluated by averaging five measurements against each sample.

The surface composition of PEG/tartrate coated MNPs is characterized by X-ray photoelectron spectroscopy (XPS) to investigate the nature of the chemisorbed surfactant molecules and to substantiate the effects of the capping agents on sample-quality, stability, and stoichiometry. Data is obtained using a SPECS XPS (monochromated Al K_α source; $h\nu = 1486.6$ eV) with

hemispherical analyser (HSA 3500). The survey scans and high-resolution elemental scans for XPS analysis are carried out with pass energy of 160 eV in steps of 1 eV and 20 eV in steps of 0.1 eV respectively. The spectra are calibrated by C 1*s* peak with a binding energy of 284.8 eV. The coordinative effect of carboxylate groups in the surface-composition is further verified by FTIR spectra, collected from Shimadzu FTIR-8400S. To analyse thermal degradation behaviour of the core-shell MNPs; about 15 mg of four chosen powder-samples are elucidated by TGA-DTG (Perkin Elmer Diamond Pyris 480) in N_2-atmosphere from room-temperature to 1000°C in 2 h. As maghemite and magnetite exhibit almost similar XRD patterns because of lookalike spinel structure, the composition is further verified by Raman spectroscopy, capable of characterizing the finger-print modes of vibration. Micro-Raman (beam-diameter ≅ 1 μm) spectrum are recorded employing a solid-state Nd:YAG laser (532.3 nm) as the excitation source and analysed by a WITec ALPHA300 RS confocal spectrometer in backscattering configuration. Holographic supernotch filters are applied to reject the Rayleigh and anti-stokes lines without using polarizers. Data is acquired using a 20X Zeiss achromatic objective with 600 groove/mm grating (spectral resolution = 3.3 cm^{-1}) by averaging 12 spectral acquisitions with 5 s of integration-time each. Laser power and data acquisition time are restricted to avoid laser-induced partial oxidation of Fe_3O_4 into maghemite, followed by hematite. Absorption spectra of the as-prepared samples are collected using a stable aqueous dispersion by employing a Shimadzu UV 3600 UV-Vis-NIR Spectrophotometer, whereas diffuse reflectance spectrum (DRS) of the commercial sample (S) is obtained using $BaSO_4$ as a reflectance standard.

Zero-field Mössbauer absorption spectra are recorded at a maximum relative speed of 14 mm s^{-1} using a constant acceleration drive (CMTE-250), equipped with a 25 mCi ^{57}Co source diffused in Rh matrix. The instrument being placed in an indigenously made vibration-free stand; is calibrated with a natural iron-foil at room temperature. Using a closed cycle refrigerator (APD Cryogenics, USA), the measurement temperature is maintained to (300.0 ± 0.5) K. The as-obtained spectra are fitted with Recoil and Fit;o) program using Lorentzian profile. Hysteresis properties of polarization are found in the Precision Premier II ferroelectric tester (maximum voltage = 10 kV) from Radiant Technologies, Inc. using standard bipolar waveform. Data is recorded at different electric fields below the breakdown strength. A KEYSIGHT InfiniiVision DSOX2012A digital storage oscilloscope is employed for the electrical data-acquisition of the as-

fabricated nanogenerators. Dielectric measurements are done using an Agilent 4294A precision impedance analyzer.

3. Characterization of MNPs

3.1. Zeta potential measurements

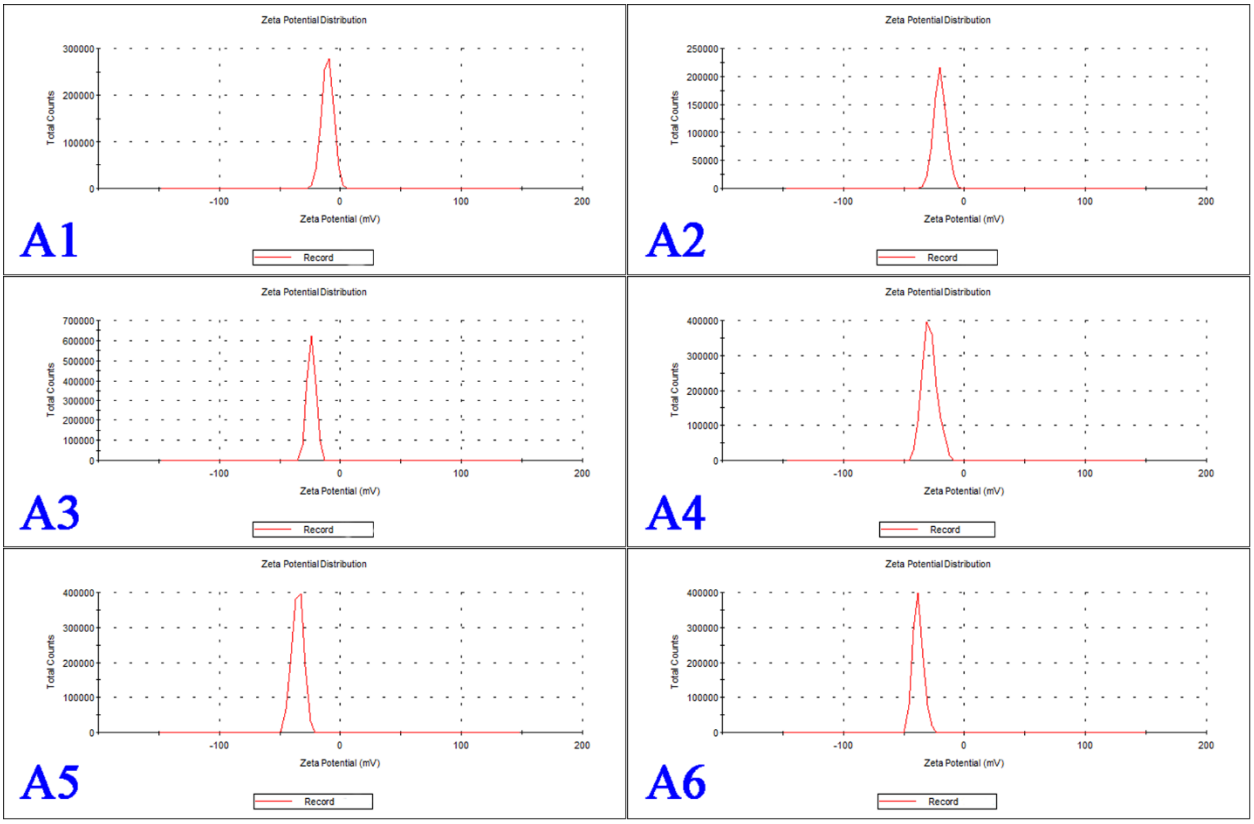

Fig. S1 Zeta potential distribution (raw data) for samples belonging to Series-A.

3.2. Fourier-transform infrared (FTIR) spectroscopy

The spectra show intense characteristic absorption peaks at 581 and 1370 cm^{-1} referring Fe-O bending & stretching vibrations respectively, see Fig. S2.[20,21] The peak at 979 cm^{-1} arise due to the bending vibrations of =C-H & C-C-O groups and the 1083 cm^{-1} peak is assigned to C-O-C axial deformation & aliphatic bending vibrations. The bands at 1598 and 1685 cm^{-1} can be attributed to –COO– stretching, bending of water molecules absorbed on the surface of MNPs and C=O stretching. The symmetric/asymmetric stretching of the methylene (=CH_2) group and C-H

stretching result the respective peaks at 2888 and 2987 cm^{-1}, whereas the bands near 3430 and 3733 cm^{-1} indicate stretching and bending vibrations of hydroxyl groups, which represent the characteristic peaks of PEG too.[20] Therefore, FTIR spectra confirms successful formation of tartrate-coated and PEGylated MNPs.

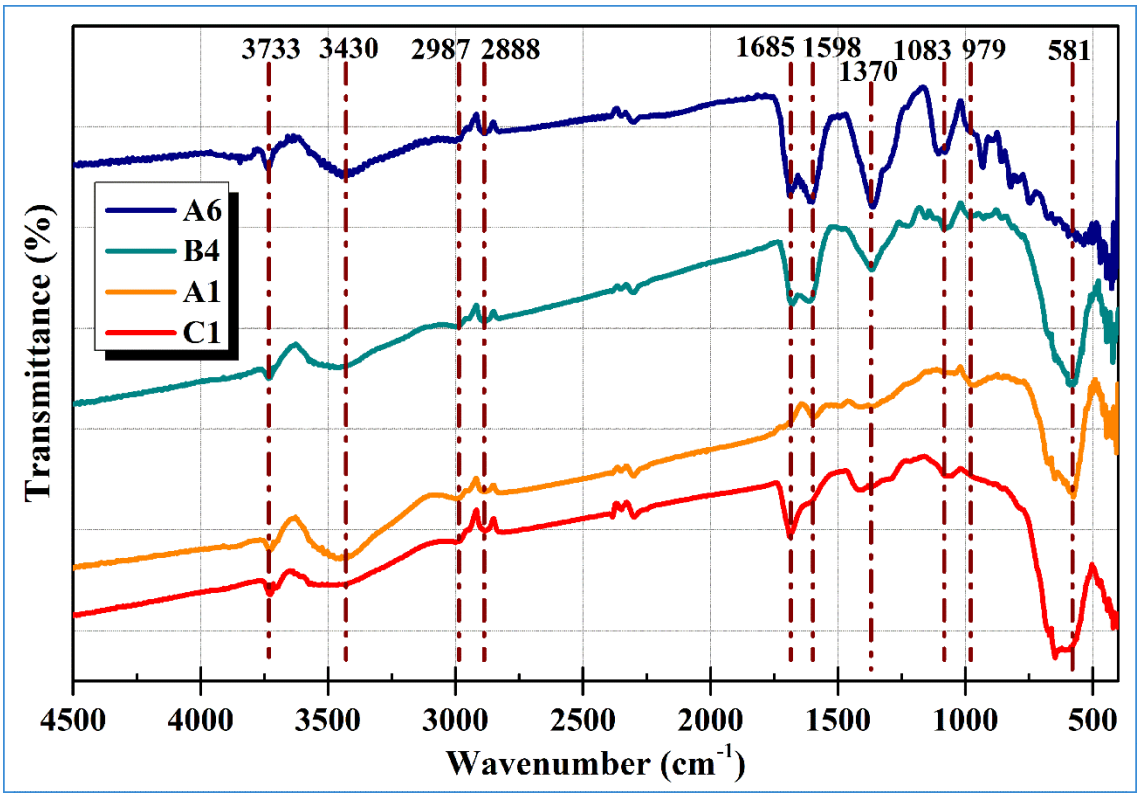

Fig. S2 FTIR spectra for four selected samples. Lattice vibrations due to specific mono- and bidentate carboxylate groups are classified for all samples.

3.3. Thermogravimetric analysis (TGA) & difference thermogravimetry (DTG)

In presence of open air or oxygen, pure Fe_3O_4 gets easily oxidized under heat-treatment and generates Fe_2O_3 polymorphs. This process gets decelerated, acted by suitable organic coating or in presence of inert atmosphere. For a quantitative overview of the carboxylate groups bound to the surface, TGA is performed in N_2-atmosphere from room-temperature to 1000°C in 2 h.

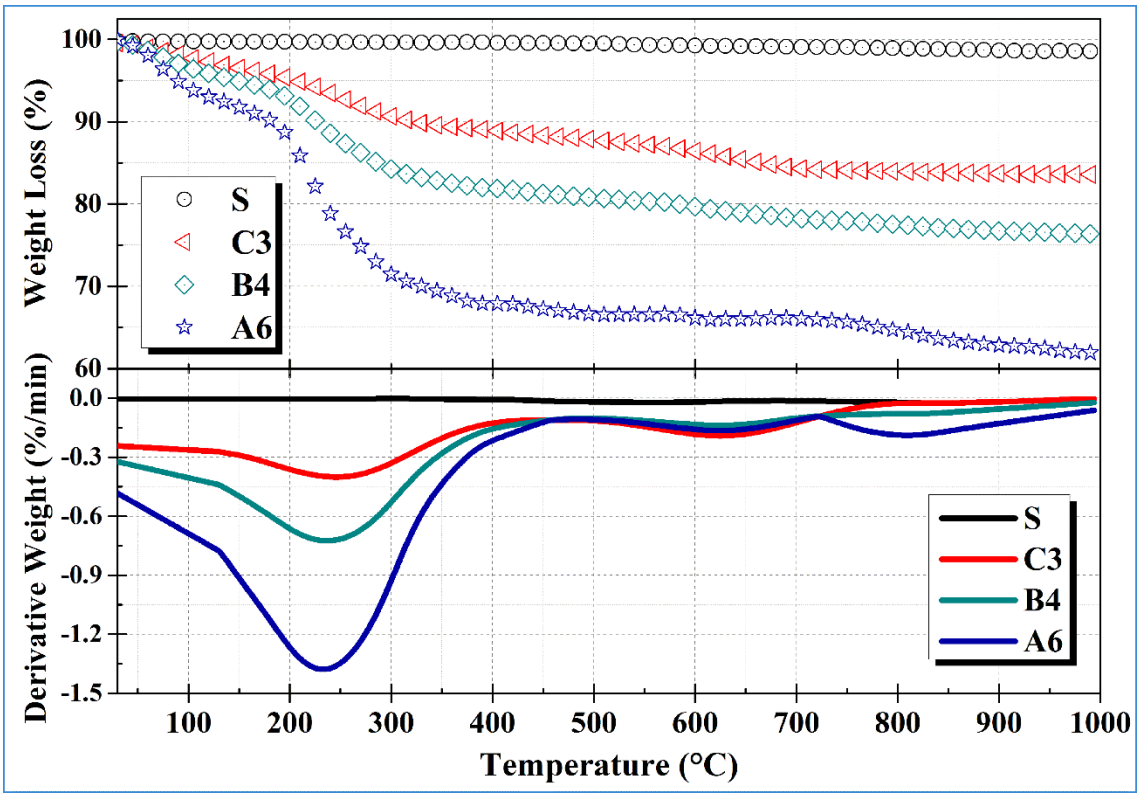

Fig. S3 TGA-DTG results in inert atmosphere for three synthesized samples in comparison with the commercial sample (S) having no surface-coating. Growth of the smaller nanoparticles is restricted by thicker coating in the core-shell structure. The organic coating gets decomposed at high temperature resulting larger weight loss; whereas the commercial sample remains intact.

As depicted in Fig. S3, a large weight loss upto 38 wt% is observed for the smallest MNPs. In contrast, much smaller loss is found for the solvothermally prepared sample (C3) with lesser amount of surfactants. The commercial sample (S) without surface-coating; produces almost no loss in N_2. It is thus demonstrated that considerable amount of carboxyl salt is bound to the surface of MNPs. The weight loss below 200°C is attributed to the adsorbed water at the surface. The main weight loss at 200–300°C is due to the decomposition of tartrate, whereas PEG undergoes a slow and steady decomposition in the range 180–900°C.[21] The small peak near 630°C might arise because of reduction to FeO, which is thermodynamically more stable than Fe_3O_4 above 570°C in phase-diagram of Fe-O system. Another tiny derivative peak near 800°C possibly signifies deoxidation of FeO in N_2 environment.

3.4. UV-Vis-NIR absorption spectroscopy

Determination of optical band-gap (Eg) from Tauc's plot is executed for all the sixteen magnetite samples under consideration. The plots are given in Fig. S4 & S5.

The variation of Urbach energy (E_u) for a number of selected samples are shown in Fig. S6. In our case, E_u depends on a number of competing factors such as crystal growth-time, concentration of surfactants, particle-size and surface to volume ratio. Decreasing reaction-time and increasing surface to volume ratio originates higher defect-density on the surface, whereas higher concentration of tartrate and PEG regularizes the growth-dynamics and controls defect-formation. Hence, although initially increases; an overall decreasing trend of E_u is observed with smaller size. The onset of absorption (E_0) on the other hand does not explicitly depend on particle-size, but firmly reciprocates the crystal-field splitting energy of the Fe_{Oct} sites.

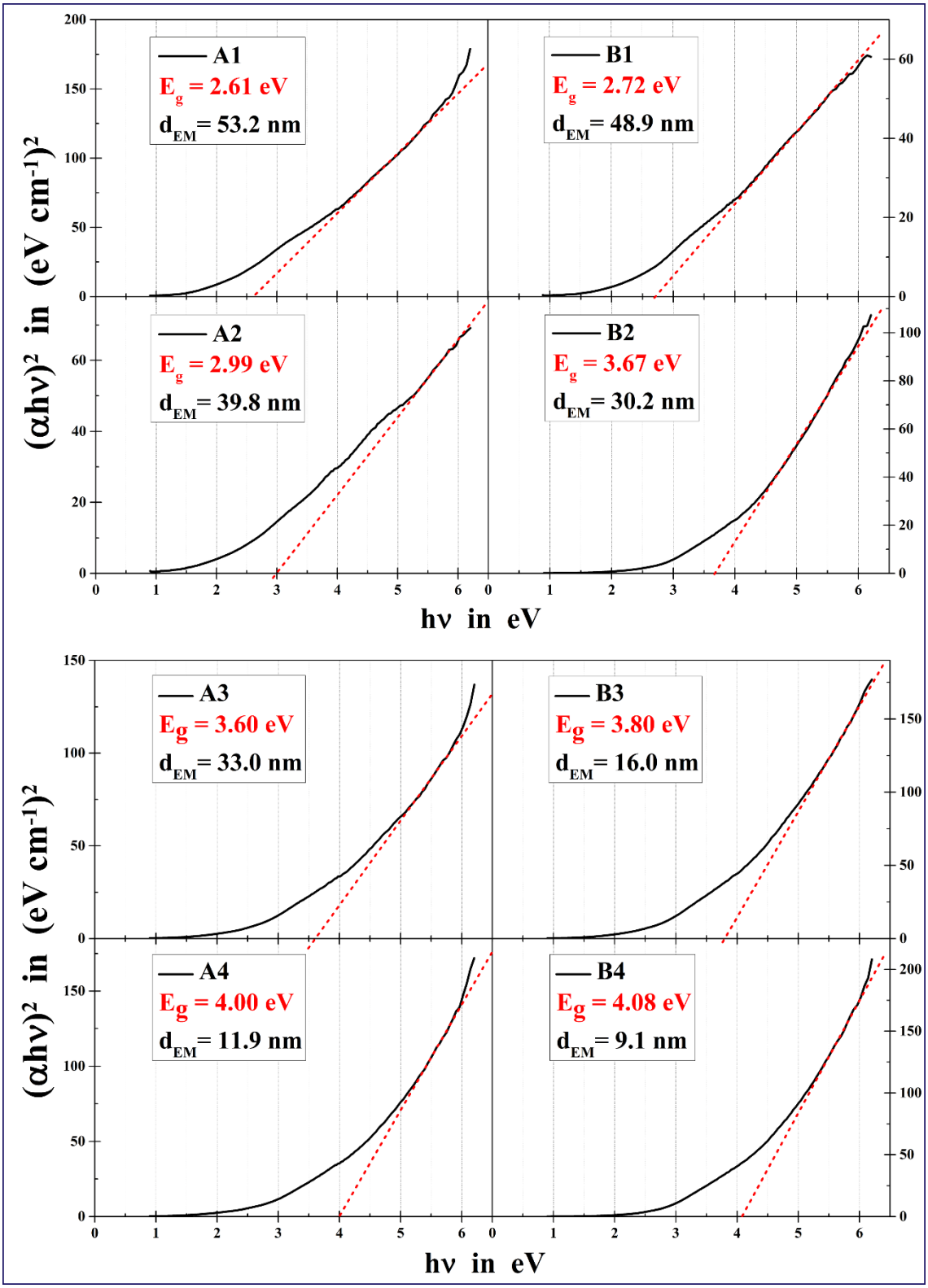

Fig. S4 Tauc's plot for samples A1 – A4 and B1 – B4.

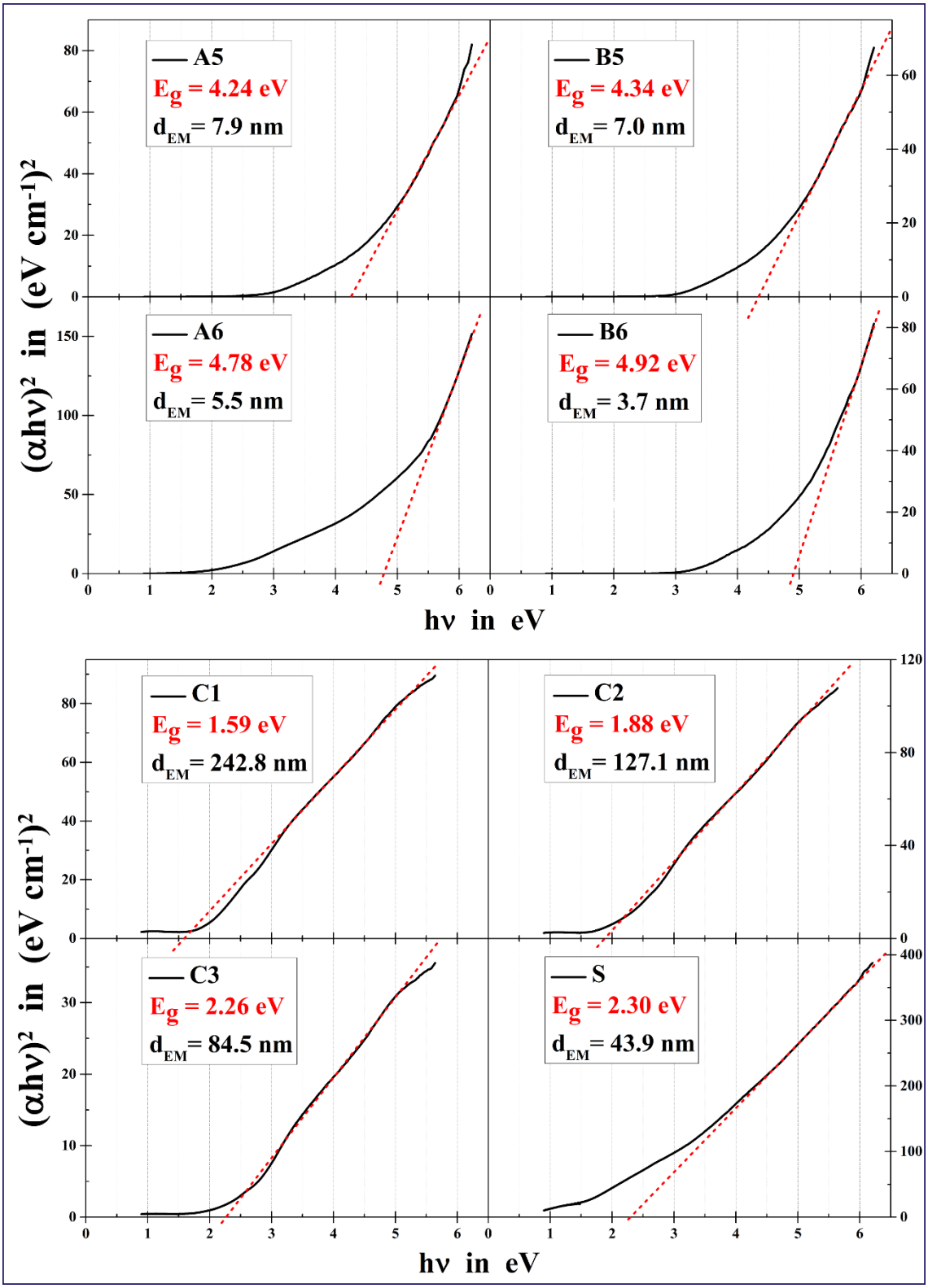

Fig. S5 Tauc's plot for samples A5 – A6, B5 – B6, C1 – C3 and S.

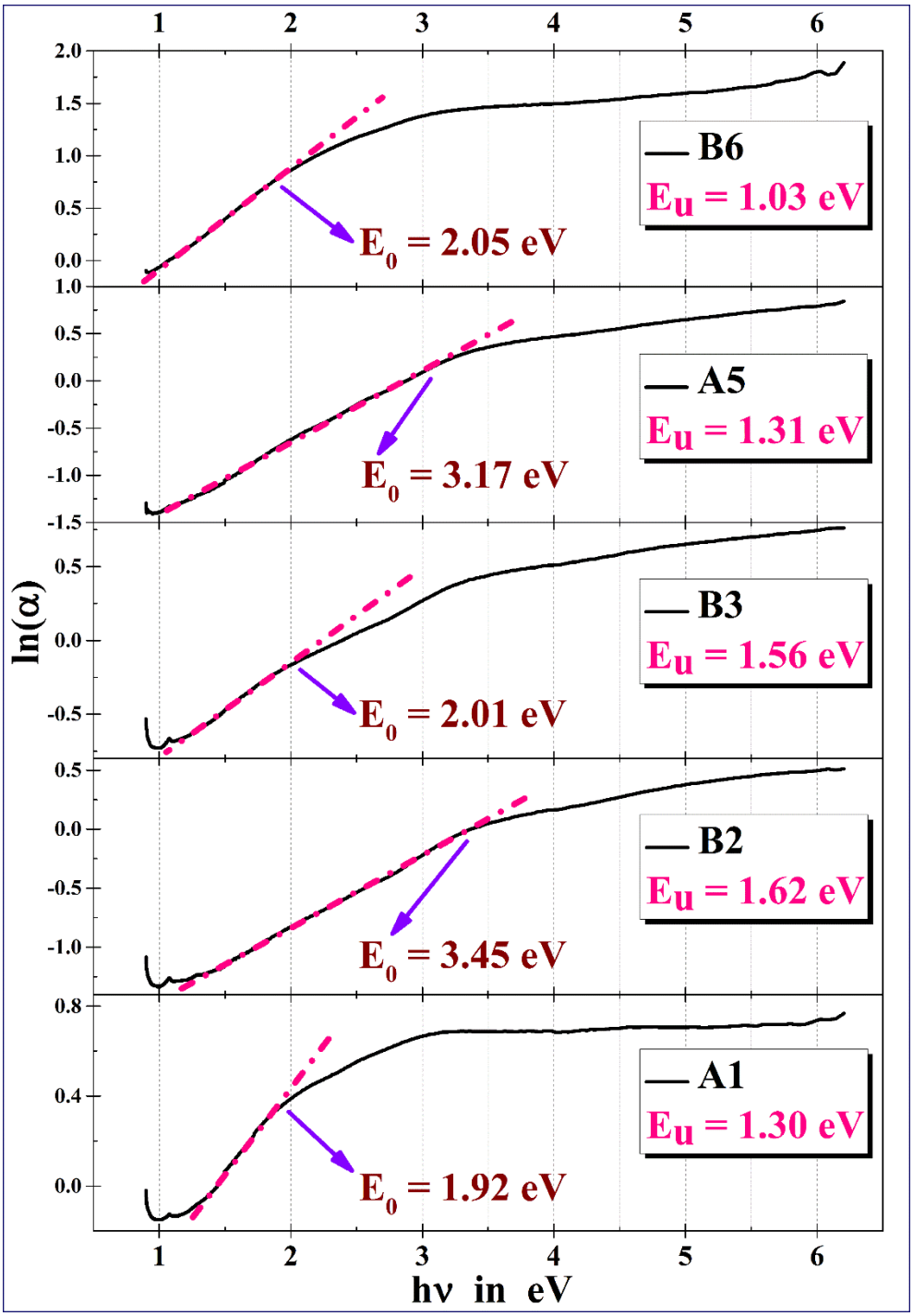

Fig. S6 Determination of Urbach energy (E_u) and the extent of exponential absorption tail (E_0) from ln α vs excitation energy ($h\nu$) plots.

4. Estimation of Fe_3O_4-PVDF electrostatic interactions from Bader charge analysis

Bader charge analysis is an intuitive method of separating a molecule to its constituent atoms by simulating the 'zero flux' surfaces. To determine the total electronic charge cumulated by an atom, charge enclosed within the conventional 'Bader volume' can be a sufficiently good approximation. Therefore, to recognise the multipole moments in the Fe_3O_4/PVDF charge-ordered nanocomposite, this technique is utilized.

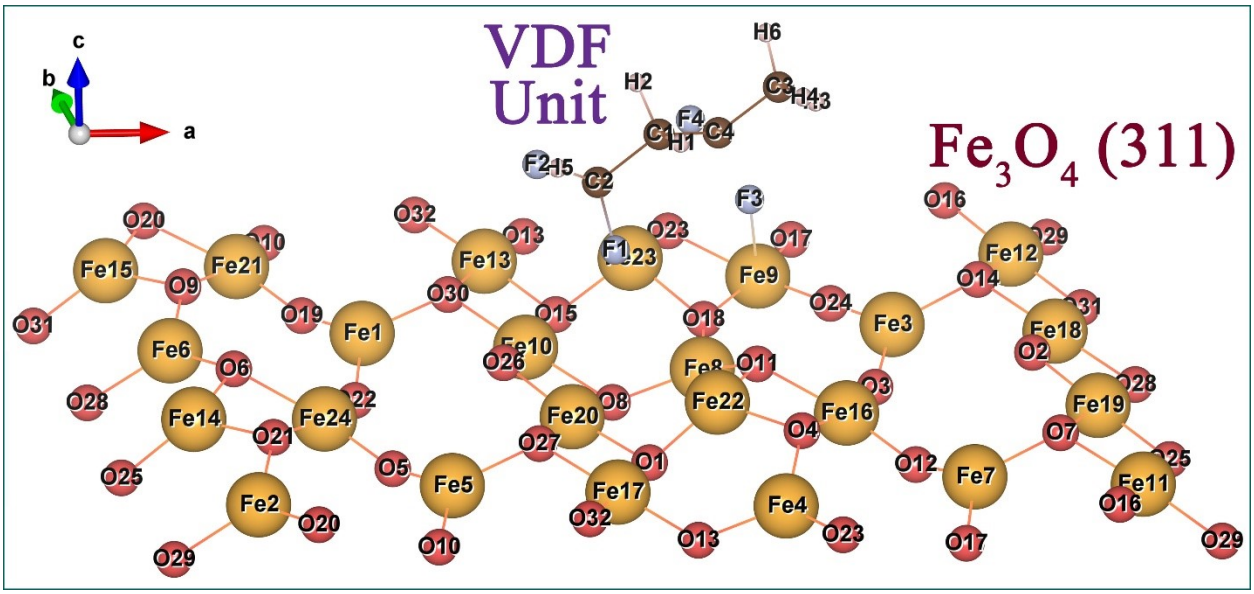

Fig. S7 All atoms, duly indexed, are demonstrated in the optimized Fe_3O_4/PVDF structure with appropriate colour-codes. The atoms have gained/lost charge according to their electronegativity to stabilize the structure and minimize free energy, conforming net dipole moment within the system.

In the following tables, charge accumulated by individual atoms in units of electronic charge are enlisted. The atoms, having direct interactions, have gone through substantial transfer of charge. Positive and negative accumulation indicate charge-loss (highlighted with blue colour) and gain (highlighted with green colour) respectively.

4.1. Charge accumulation in Fe_3O_4

Table S2. Bader charge garnered in Fe and O atoms on (311) plane of Fe_3O_4

Indexed Fe atoms	Total accumulated charge (in e^-)	Indexed O atoms	Total accumulated charge (in e^-)
Fe1	1.57602	O1	-1.20837
Fe2	1.44452	O2	-0.99048
Fe3	1.4858	O3	-1.0329
Fe4	1.50617	O4	-1.23273
Fe5	1.55805	O5	-0.98333
Fe6	1.44921	O6	-1.21227
Fe7	1.60166	O7	-1.15993
Fe8	1.50774	O8	-1.17506
Fe9	1.68398	O9	-1.19963
Fe10	1.58685	O10	-1.03815
Fe11	1.53842	O11	-1.23585
Fe12	1.55125	O12	-1.05427
Fe13	1.60675	O13	-1.17886
Fe14	1.39391	O14	-1.14536
Fe15	1.37256	O15	-1.18667
Fe16	1.58513	O16	-1.00225
Fe17	1.53357	O17	-1.04785
Fe18	1.48923	O18	-1.18649
Fe19	1.51235	O19	-1.02455
Fe20	1.55184	O20	-1.20901
Fe21	1.51443	O21	-1.21176
Fe22	1.37111	O22	-0.9841
Fe23	1.50939	O23	-1.20103
Fe24	1.45837	O24	-0.9903
		O25	-1.23438

	O26	-0.99711
	O27	-1.18198
	O28	-1.15643
	O29	-1.16415
	O30	-1.13464
	O31	-1.20319
	O32	-0.98527

4.2. Charge accumulation in PVDF

Table S3. Bader charge garnered in C, H, and F atoms

Indexed C/H/F atoms	Total accumulated charge (in e^-)
C1	0.03625
C2	0.7196
C3	0.07376
C4	1.31349
H1	0.05024
H2	0.06033
H3	0.04305
H4	0.02139
H5	0.10515
H6	0.02809
F1	-0.75495
F2	-0.55329
F3	-0.76024
F4	-0.82283

5. Further investigation on Fe_3O_4/PVDF nanocomposites

5.1. Quantitative assessment of β-phase from FTIR analysis

FTIR analysis is the most abundantly used method to quantify all the electroactive phase-contents present in PVDF, although different researchers have performed such quantifications using versatile formulae following distinct distributions. As XRD and Raman spectra hint that, the γ-phase content is nominal and hardly differs against MNP-incorporation; the β-phase can be considered as the only major electroactive phase present in the system. Assuming that the FTIR absorption spectra follows the Beer-Lambert law, the following formula, used by several researchers[22-25] is employed to calculate the relative fraction of the β-phase with respect to the non-polar α-phase:

$$F(\beta) = \frac{A_\beta}{\left(\frac{K_\beta}{K_\alpha}\right) A_\alpha + A_\beta} X100\% \qquad \text{(S1)}$$

where $F(\beta)$ is the exact β-content in percentage, A_α & A_β are the absorbance-values for the two phases and $K_\alpha(= 6.1X10^4\ cm^2\ mol^{-1})$ & $K_\beta(= 7.7X10^4\ cm^2\ mol^{-1})$ are the absorption coefficients at the respective wavenumber of 764 & 844 cm^{-1}, which are the most prominent signatures of the associated phases. Using this formula, β-content is graphically presented as a function of both MNP-size and wt (%) in Fig. S8. The results show high improvement in electroactive fraction (from 10.9% to 71.4%) against incorporation of MNPs, which is in agreement with the results obtained from the Raman analysis given in the main manuscript.

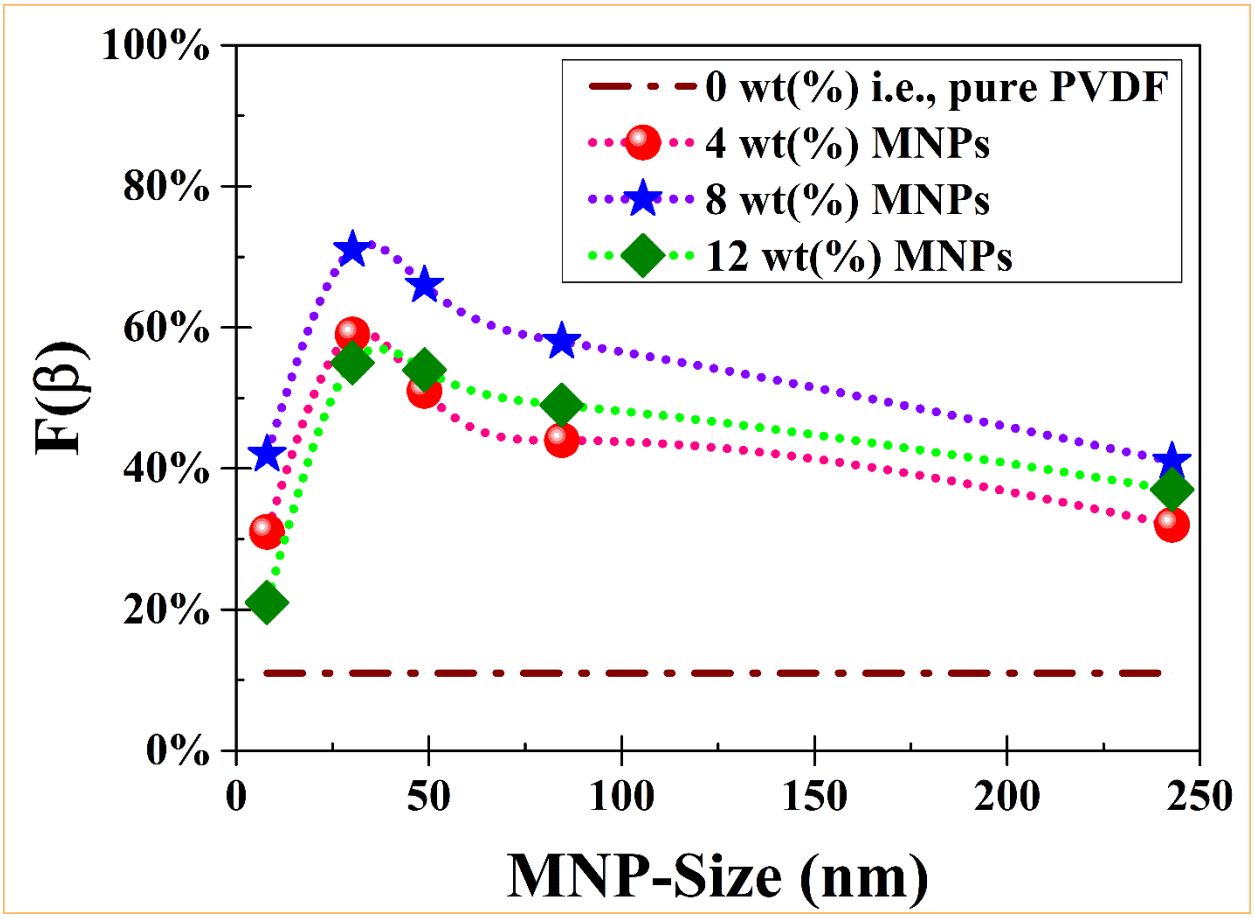

Fig. S8 Quantitative comparison of β-phase content obtained from FTIR spectra for incorporation of MNPs with different size and weight ratio. The dotted lines are guide to the eye. The curves show, 30.2 nm MNPs at 8 wt(%) addition holds optimum results. Deviation from these parameters entails lesser enhancement.

5.2. Dielectric spectroscopy

Dielectric spectroscopy is a useful characterization tool to assess electrical energy storing capacity of a system. Frequency-dispersion of the dielectric constant (ε_r) is obtained from the capacitance values (C), using the following formula,

$$\varepsilon_r = \frac{\varepsilon}{\epsilon_0} = \frac{Ct}{\epsilon_0 A} \qquad \text{(S2)}$$

where t = thickness of the film, ϵ_0 = permittivity of vacuum = 8.854 × 10^{-12} F m^{-1} and A is the effective electrode area. As the MNPs are incorporated in PVDF, not only the dielectric constant (both static value and high frequency behaviour) enhances, but also the overall dipolar relaxation gets reshaped as shown in Fig. S9. This signifies notable electroactive phase formation inside the nanocomposites.[26]

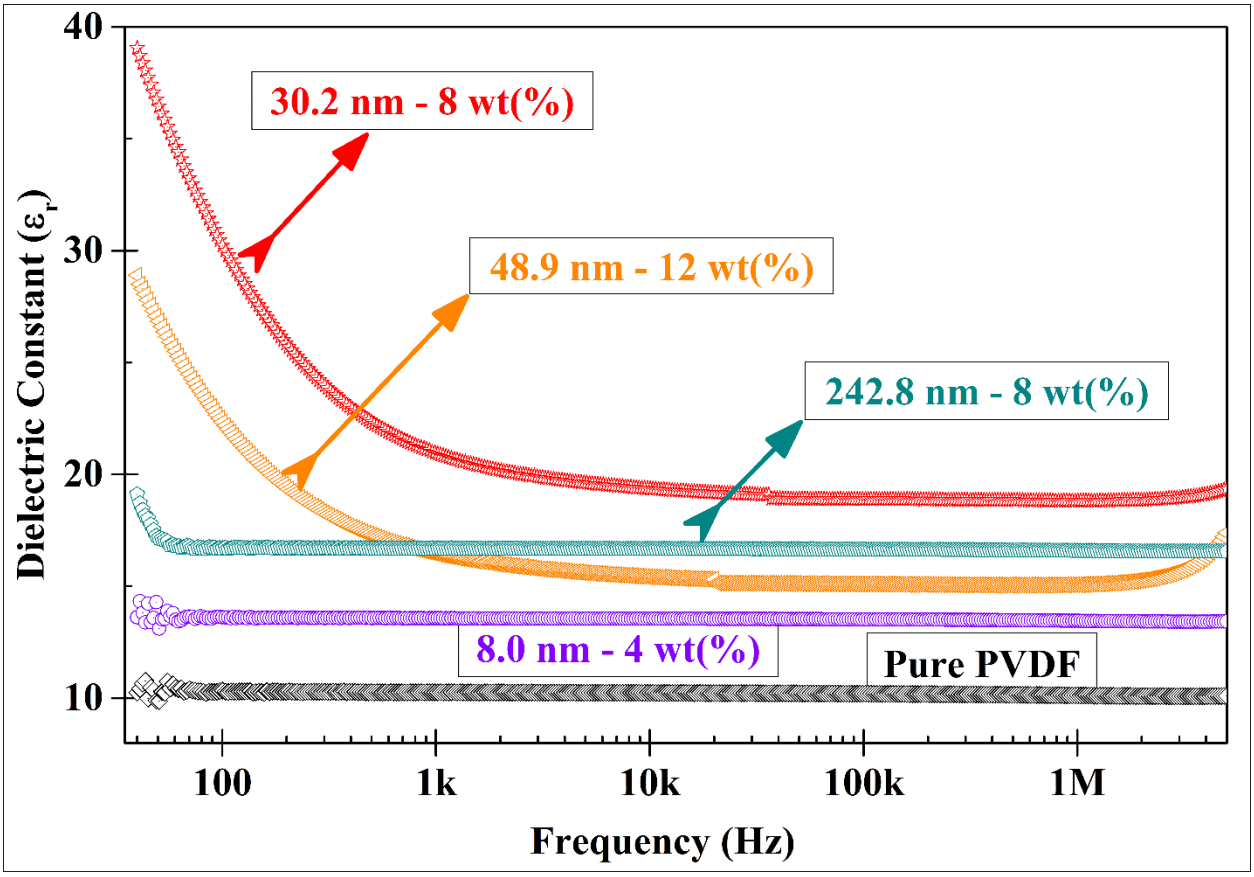

Fig. S9 Dielectric dispersion for five selected samples, showing considerable increase in the polarization behaviour and dielectric constant.

6. References

1. G. Wang, X. Zhang, A. Skallberg, Y. Liu, Z. Hu, X. Mei and K. Uvdal, *Nanoscale*, 2014, **6**, 2953-2963.
2. M. Abboud, S. Youssef, J. Podlecki, R. Habchi, G. Germanos and A. Foucaran, *Mat. Sci. Semicon. Proc.*, 2015, **39**, 641-648.
3. O. Lemine, K. Omri, B. Zhang, L. El Mir, M. Sajieddine, A. Alyamani and M. Bououdina, *Superlattice. Microst.*, 2012, **52**, 793-799.
4. Z. Li, H. Chen, H. Bao and M. Gao, *Chem. Mater.*, 2004, **16**, 1391-1393.
5. D. Caruntu, G. Caruntu, Y. Chen, C. J. O'Connor, G. Goloverda and V. L. Kolesnichenko, *Chem. Mater.*, 2004, **16**, 5527-5534.
6. C.-H. Ho, C.-P. Tsai, C.-C. Chung, C.-Y. Tsai, F.-R. Chen, H.-J. Lin and C.-H. Lai, *Chem. Mater.*, 2011, **23**, 1753-1760.
7. I. Karimzadeh, H. R. Dizaji and M. Aghazadeh, *Mater. Res. Express*, 2016, **3**, 095022.
8. L. Zhuang, W. Zhang, Y. Zhao, H. Shen, H. Lin and J. Liang, *Sci. Rep.*, 2015, **5**, 9320.
9. J. Chen, K. Huang and S. Liu, *Electrochim. Acta*, 2009, **55**, 1-5.
10. M. Jean, V. Nachbaur and J.-M. Le Breton, *J. Alloys Compd.*, 2012, **513**, 425-429.
11. E. Aivazoglou, E. Metaxa and E. Hristoforou, *AIP Adv.*, 2018, **8**, 048201.
12. C. Li, Y. Wei, A. Liivat, Y. Zhu and J. Zhu, *Mater. Lett.*, 2013, **107**, 23-26.
13. Y. J. Liang, Y. Zhang, Z. Guo, J. Xie, T. Bai, J. Zou and N. Gu, *Chem.: Eur. J.*, 2016, **22**, 11807-11815.
14. N. Zhu, H. Ji, P. Yu, J. Niu, M. Farooq, M. W. Akram, I. Udego, H. Li and X. Niu, *Nanomaterials*, 2018, **8**, 810.
15. M. Mascolo, Y. Pei and T. Ring, *Materials*, 2013, **6**, 5549-5567.
16. Y.-w. Jun, Y.-M. Huh, J.-s. Choi, J.-H. Lee, H.-T. Song, S. Kim, S. Kim, S. Yoon, K.-S. Kim and J.-S. Shin, *J. Am. Chem. Soc.*, 2005, **127**, 5732-5733.
17. S. Schwaminger, D. Bauer, P. Fraga-García, F. Wagner and S. Berensmeier, *CrystEngComm*, 2017, **19**, 246-255.
18. L.-h. Shen, J.-f. Bao, D. Wang, Y.-x. Wang, Z.-w. Chen, L. Ren, X. Zhou, X.-b. Ke, M. Chen and A.-q. Yang, *Nanoscale*, 2013, **5**, 2133-2141.
19. S. Bhattacharjee, *J. Control. Release*, 2016, **235**, 337-351.

20. S. Bhattacharjee, A. Banerjee, N. Mazumder, K. Chanda, S. Sarkar and K. K. Chattopadhyay, *Nanoscale*, 2020, **12**, 1528-1540.
21. V. Panwar, P. Kumar, A. Bansal, S. S. Ray and S. L. Jain, *Appl. Catal. A-Gen.*, 2015, **498**, 25-31.
22. P. Martins, A. Lopes and S. Lanceros-Mendez, *Prog. Polym. Sci.*, 2014, **39**, 683-706.
23. M. Pusty, L. Sinha and P. M. Shirage, *New J. Chem.*, 2019, **43**, 284-294.
24. J. Gregorio, Rinaldo and M. Cestari, *J. Polym. Sci. B: Polym. Phys.*, 1994, **32**, 859-870.
25. T. U. Patro, M. V. Mhalgi, D. Khakhar and A. Misra, *Polymer*, 2008, **49**, 3486-3499.
26. V. Jella, S. Ippili, J.-H. Eom, J. Choi and S.-G. Yoon, *Nano Energy*, 2018, **53**, 46-56.

= =